Available online at www.sciencedirect.com

ScienceDirect

journal homepage: www.elsevier.com/locate/he

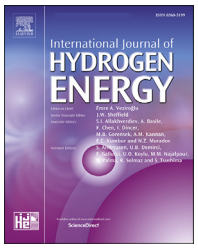

Exsolution of Ni nanoparticles on the surface of cerium and nickel co-doped lanthanum strontium titanate as a new anodic layer for DIR-SOFC. Anti-coking potential and H_2S poisoning resistance of the prepared material

Patryk Błaszczak [a,*], *Marcin Łapiński* [a], *Sea-Fue Wang* [b], *Piotr Jasiński* [c], *Beata Bochentyn* [a]

[a] *Advanced Materials Center, Faculty of Applied Physics and Mathematics, Gdansk University of Technology, 80-233, Gdańsk, Ul. Narutowicza 11/12, Poland*

[b] *Department of Materials and Mineral Resources Engineering, National Taipei University of Technology, 1, Sec. 3, Zhongxiao E. Rd., Taipei, 106, Taiwan*

[c] *Advanced Materials Center, Faculty of Electronics, Telecommunications and Informatics, Gdansk University of Technology, 80-233, Gdańsk, Ul. Narutowicza 11/12, Poland*

HIGHLIGHTS

- $La_{0.27}Sr_{0.54}Ce_{0.09}Ni_{0.1}Ti_{0.9}O_{3-\sigma}$ (LSCNT) anodic layer for DIR-SOFC was prepared.
- Performance in hydrogen, synthetic and sulfur-contaminated biogas was examined.
- Anode with LSCNT layer is more stable and lowers the overall cell degradation.

ARTICLE INFO

Article history:
Received 18 April 2020
Received in revised form
16 July 2020
Accepted 17 July 2020
Available online 20 August 2020

Keywords:
SOFC
Biogas
Reforming
Exsolution
Strontium titanate
FTIR

ABSTRACT

The aim of this study was to evaluate a new catalytic material for biogas-fuelled DIR-SOFCs. This material was a perovskite-type $SrTiO_3$ doped with La, Ce and Ni of a general formula $La_{0.27}Sr_{0.54}Ce_{0.09}Ni_{0.1}Ti_{0.9}O_{3-\sigma}$ (LSCNT). Additional preparation steps were undertaken to promote a nickel exsolution process. Heat post-treatment of powders in a humidified H_2 resulted in an intensive growth of nickel nanoparticles (NPs) while the reduction temperature was increased gradually from 800 to 1200 °C. A selected reduction temperature equal to 900 °C gave the NPs an average size of 22 nm. The prepared material was used as a functional layer deposited onto the anodic site of a Ni/YSZ-supported SOFC to promote the effective reforming of synthetic and H_2S-contaminated biogas at 750 °C. It was found that after 130 h of operation in a 60% CH_4/40% CO_2 mixture, the fuel cell with an additional LSCNT layer showed higher power density, and no carbon deposits were observed. However, 20 ppm of H_2S present in the fuel caused a full deactivation of both the reference and SOFC with LSCNT layer. Cyclic tests in sour biogas revealed that the fabricated anodic layer is much more resistant to sulfur poisoning compared to a bare Ni/YSZ anode. Recovery of overall performance after 3 poisoning cycles was nearly 90% for the fuel cell with the LSCNT layer, while the unmodified one reached only 75%. The concentrations

* *Corresponding author.*
E-mail address: patryk.blaszczak@pg.edu.pl (P. Błaszczak).

https://doi.org/10.1016/j.ijhydene.2020.07.162

of the exhaust gases, such as CH_4, CO_2, and CO, were continuously measured *in situ* using a FTIR-based technique. A thermochemical analysis revealed that the investigated material ensured much better biogas reforming stability over the whole testing time and strongly promoted catalytic reactions.

Introduction

Nowadays, more and more effort is being put into environmentally friendly and sustainable energy sources. Widely examined Direct Internal Reforming Solid Oxide Fuel Cells (DIR-SOFCs) are promising candidates when it comes to harvesting electricity for industry, public buildings, and private housing. These can provide clean energy with enormously high efficiency. Their all-solid-type construction ensures higher mechanical resistivity and reliability. Hydrogen as an essential fuel for SOFCs is dangerous in storage, and its production is still challenging and undoubtedly not cost-effective. To overcome these issues, new sources of hydrogen have to be used [1–7]. One of the examples are hydrocarbons such as methane (CH_4), which can undergo so-called reforming reactions. The most common reactions are listed in Eqs. (1)–(7) [8].

Dry reforming $$CH_4 + CO_2 \leftrightarrow 2CO + 2H_2 \quad (1)$$

Steam reforming $$CH_4 + H_2O \leftrightarrow CO + 3H_2 \quad (2)$$

(RWGS) Reverse Water – Gas Shift reaction $$CO_2 + H_2 \leftrightarrow CO + H_2O \quad (3)$$

Methanation $$CO_2 + 4H_2 \leftrightarrow CH_4 + 2H_2O \quad (4)$$

Methane pyrolysis $$CH_4 \leftrightarrow C + 2H_2 \quad (5)$$

Boudouard reaction $$2CO \leftrightarrow C + CO_2 \quad (6)$$

CO reduction $$CO + H_2 \leftrightarrow C + H_2O \quad (7)$$

Unfortunately, the widely used Ni/YSZ cermet anodes easily undergo carbon coking while working in systems fed with hydrocarbons. The mentioned process causes the accumulation of severe carbon forms on the active sites of Ni particles, which are used as catalytic centres for reforming reactions of, e.g. methanol and methane. Additionally, in bio-based fuels, such as biogas, a trace amount of H_2S is always present. Hydrogen sulphide, even in small amounts, degrades metallic Ni particles by the formation of a chemically inactive Ni_xS_y. Both phenomena lead to the lowering of the overall performance of the fuel cell, and finally, to irreversible breakdown [9–14].

Many scientific papers have been published to date concerning perovskites as potential anodic materials for SOFC construction. There is special interest in oxide anodes, which are able to undergo the exsolution process of B-site cations, producing highly stable and electrocatalytically active nanoparticles embedded in the perovskite [15–18]. Based on this, a novel perovskite-type material was designed and introduced as a good candidate to become an additional anodic layer in SOFCs. A schematic concept of the LSCNT compound working under a biogas atmosphere is presented in Fig. 1. La-, Ce- and Ni-doped $SrTiO_3$ are predicted to fuse the advantages of all of its elements. Strontium titanate ensures chemical stability [19], and La ions increase the compound's electrical conductivity [20,21]. Additional doping with Ce should intensify the carbon gasification and sulfur poisoning due to the tendency of cerium ions to easily switch between 3+ and 4+ valence states [22]. Ni ions introduced into the B-site sublattice are meant to undergo the exsolution process resulting in metallic NPs, being catalytic centres for reforming reactions [23,24]. An additional functional layer consisting of LSCNT deposited onto the anodic side of a NiO-YSZ/YSZ/LSM-YSZ planar fuel cell should increase the overall efficiency of biogas reforming due to the highly dispersed nickel nanoparticles and ensuring stable work due to the $SrTiO_3$ matrix. According to previous work of Y. *Sun* [25], a $La_{0.3}Sr_{0.6}Ce_{0.1}Ni_{0.1}Ti_{0.9}O_{3-\sigma}$ compound highly increased the stability of a SOFC working under H_2/H_2S feeding. In this work, an A-site deficient LSCNT compound was synthesised in such a way as to intensify the Ni exsolution process, and was tested also under a sour biogas atmosphere. The aim of presented work was to examine LSCNT material for its catalytic activity at a working temperature of 750 °C, study the Ce doping effects, and test the mechanical integration with a SOFC in order to displace the widely-known Ni/YSZ cermet with $SrTiO_3$-based compounds.

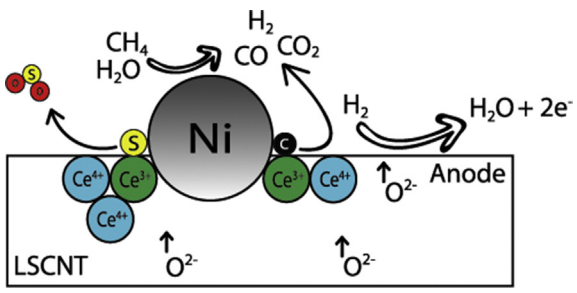

Fig. 1 – Schematic concept of processes in LSCNT anodic material.

Experimental

Synthesis of the LSCNT compound

$La_{0.27}Sr_{0.54}Ce_{0.09}Ni_{0.1}Ti_{0.9}O_{3-\sigma}$ (LSCNT) was synthesised using the Pechini method. Appropriate amounts of metal nitrates $La(NO_3)_3 \cdot 6H_2O$ (Sigma-Aldrich/Merck, 99.99%), $Sr(NO_3)_2$ (Pol-Aura, 99%), $Ce(NO_3)_3 \cdot 6H_2O$ (Sigma-Aldrich/Merck, 99%), and $Ni(NO_3)_2 \cdot 6H_2O$ (Sigma-Aldrich/Merck, 99%) were weighed and dissolved in DI water to create a 30% salt solution. In another beaker, a stoichiometric amount of titanium (IV) butoxide ($Ti(OBu)_4$, Merck, 97%) was mixed together with reagent-grade ethylene glycol (EG), and citric acid (CA) in a molar ratio equal to 2:1 until a white slurry was obtained. The water-based solution was then added to a titanium precursor mixture and stirred at 80 °C until fully dissolved. After this, the solution was heated to 150 °C and condensed until gel was obtained. Next, the gel was transferred into an alumina crucible and calcined for 1 h at 400 °C, and then for 1 h at 600 °C. Finally, the yellowish powder was ground and sintered a temperatures ranging from 800 °C to 1200 °C for 12 h under an air atmosphere. To perform exsolution of Ni NPs, the prepared powders were heat-treated again in the stream of a humid H_2 (3% H_2O) at 800, 900, 1000, 1100, or 1200 °C.

Deposition of a functional layer

The fabricated LSCNT powder was ground together with ESL 403 organic binder until a uniform, highly viscous paste was obtained. Layers were deposited using a screen printing technique onto the anodic surface of a SOFC prepared using tape casting. The delivered fuel cell consisted of a 440 μm NiO/YSZ anode with two levels of porosity, a 10 μm YSZ electrolyte, and a 30 μm LSM/YSZ cathode with a specific surface area equal to 1.13 cm^2. The LSCNT layer was screenprinted, dried for 12 h at 80 °C, and sintered for 2 h at 1100 °C under an air atmosphere.

Measurement techniques

The phase composition was determined by an X'Pert Pro MPD Philips diffractometer using $Cu_{K\alpha}$ ($\lambda = 1.542$ Å) radiation at room temperature. The size and uniformity of the NPs, as well as the morphology of the powders, were verified after each reduction process using a Scanning Electron Microscope (SEM, FEI Quanta FEG 250) with an Energy Dispersive X-ray spectroscope (EDX, EDAX Genesis APEX 2i), and an Apollo X SDD detector operating at 15 kV. An X-ray Photoelectron Spectroscopy analysis (XPS) was performed using an X-ray photoelectron spectrometer (Omnicron NanoTechnology) with a 128-channel collector. XPS measurements were undertaken under ultra-high vacuum conditions, below 1.1×10^{-8} mbar. Photoelectrons were excited by an Mg-Kα X-ray source with the X-ray anode operated at 15 keV and 300 W. The thermal expansion coefficient was examined using a Netzsch DIL 402 PC dilatometer working in the 100–1000 °C temperature range in an air atmosphere at a 3 °C/min heating/cooling rate.

The measurement of the electrical properties, simultaneously with an analysis of the concentration of the outlet gases from the operating SOFC, were performed using a specially dedicated unit described in detail in our previous work [11]. In brief, the electrical properties of the fuel cell were measured using Gamry potentiostat/galvanostat. Gold wires were connected to the anode side using silver paste to ensure no contribution to electrochemical performance. A tubular furnace with the mounted fuel cell was heated in a flux of 40 mL min^{-1} N_2 to 900 °C. After this, the gas was switched to H_2 for 10 h in order to perform an exsolution process. The temperature of the exsolution process (900 °C) was selected based on the initial reduction investigations presented in this work. Next, the temperature was decreased to 750 °C, and the fuel cell's initial performance in H_2 was examined for 12 h. Next, the feeding fuel was changed to 30 mL min^{-1} of humidified synthetic biogas mixture (60% CH_4/40% CO_2 by vol. with around 3% of H_2O). The gas flow rates were set to ensure a continuous flow of the feeding gas to the SOFC anode. This study was focused more on a comparison of the activity of the additional LSCNT layer and its influence on the degradation rate, disregarding the optimal fuel utilisation factor discussed in other papers [26,27]. The current density vs. time at a static load of 0.65 V, and current-voltage measurements were performed both in H_2 and synthetic biogas. Due to the introduction of significant instability of the SOFC's performance while switching from potentionstatic to impedance measurements, the authors decided to exclude this step.

Additional tests in sour, humidified biogas containing 20 ppm of H_2S were also performed. After initial reduction and 12 h of operating in hydrogen, the fuel cell was periodically fed with H_2S-contaminated biogas for 8 h with a continuous examination of the changes in the electrical properties. After each poisoning cycle, H_2 was supplied for 12 h to determine the level of irreversible degradation caused by the H_2S.

While pending the electrical measurements, the concentrations of CO, CO_2, and CH_4 in the exhaust gases were monitored *in situ* using the FTIR spectrometer-based method described in detail in our previous work [11]. Keeping in mind the many limitations of using FTIR for measuring gas concentrations, the set-up was developed in such a way as to minimise the known errors. Similar units were proposed earlier, and allowed valuable results to be obtained [28,29]. The gas cell was heated up to 60 °C, which improved the baseline stability. The flow of exhaust gases was also monitored using an additional flow meter. FTIR spectra were collected every 10 min within the wavenumber range of 4000–500 cm^{-1} with a resolution of 4 cm^{-1}. An additional correction coming from gas retention in the sampling line was also introduced. Based on the changes in the concentrations of each gas, the catalytic parameters for the SOFC working in synthetic biogas were calculated. They are the CH_4 and CO_2 conversion rates, the CO and H_2 yields, and the CO and H_2 selectivities [11].

Chemical non-equilibrium analysis

To determine which direction the reaction is most likely to proceed in, the reaction quotients (Q_r) were calculated. These calculations were done for the fuel cells working in synthetic

biogas only. To extract information about the possibility of solid carbon formation, the carbon activity coefficients $\alpha_{C,r}$ were obtained as a reciprocal of Q_r. The detailed procedure of non-equilibrium analysis of reforming reactions using changes of the Q_r and $\alpha_{C,r}$ values in time was described in our previous paper [11]. Due to water removal from the measured output mixture, its amount was estimated according to a mass-atom balance of hydrogen and oxygen, considering also the oxygen ions pumped through the electrolyte during operation of the SOFC, calculated based on Faraday's law (as CO is not usually oxidised at the anode [30]). The calculations were done assuming each process happens independently given the high complexity of the undergoing reactions.

Results

Phase composition of LSCNT

XRD patterns of the fabricated material after the sintering step at different temperatures are presented in Fig. 2. It can be clearly seen that the precursor sintered at 1200 °C became a single-phase material revealing full substitution of Sr and Ti lattice positions with La/Ce and Ni ions, respectively. In the other cases, additional phases such as CeO_2, $NiTiO_3$, and NiO can be found.

Referring to the paper of Y. *Sun* et al. [25], it is highly likely that an A-site deficiency ($A_{0.9}BO_3$) allowed Ce ions to build into a host lattice more easily. As a result, no CeO_2 is observed after the sintering in an air atmosphere. To prove the given statement, an additional stoichiometric (ABO_3) sample of $La_{0.3}Sr_{0.6}Ce_{0.1}Ni_{0.1}Ti_{0.9}O_{3-\sigma}$ was prepared for comparison. The XRD patterns of the ABO_3 and $A_{0.9}BO_3$ samples are presented in Fig. 3. As in the results of Y. *Sun* et al. [25], a CeO_2 phase was clearly visible in the stoichiometric compound after the sintering step conducted in the air (1200 °C).

Based on the XRD data, the LSCNT lattice parameters were calculated using the Rietveld refining method. The results are presented in Table 1. The doped compound maintained the cubic perovskite phase. A slight decrease in the lattice parameter of the doped $SrTiO_3$ occurred due to the smaller ionic radii of XII-coordinated La^{3+} and Ce^{4+} compared to the radius of a Sr^{2+} ion [30,31]. On the other hand, changes in the lattice parameter caused by A-site dopants were counterbalanced by VI-coordinated Ni^{2+} ions present in the B sublattice (0.69 Å for Ni^{2+} vs. 0.605 Å for Ti^{4+} [32]) as well as the electronic effects of La doping into $SrTiO_3$ [33].

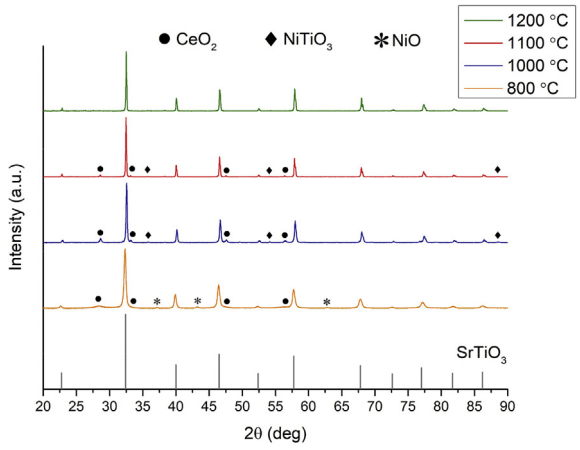

Fig. 2 – XRD patterns of LSCNT precursor sintered at different temperatures. All unmarked peaks correspond to $SrTiO_3$ cubic phase (see $SrTiO_3$ calculated XRD pattern).

To determine the oxidation states of La, Sr, Ce, Ni, and Ti in the synthesised compound, the XPS spectra were collected and analysed. The results are presented in Fig. 4.

The results presented in Fig. 4A–D revealed that all of the dopants were incorporated into the $SrTiO_3$ lattice as expected. On the basis of the XPS spectra of the La3d, Ni2p, and Ti2p regions (Fig. 4A and B), the presence of La^{3+}, Ni^{2+}, and Ti^{4+} cations was confirmed. No other valence states were detected. The Sr3d spectrum (Fig. 4C) is characteristic of Sr^{2+}. Deconvolution of the XPS results exhibit two forms of strontium on the surface of the sample: the Sr in $SrTiO_3$, and a small amount of Sr^{2+} in the form of SrO [34]. The material exhibited surface SrO-termination. This is a well-known behaviour of $SrTiO_3$-based compounds, which has been previously studied [35–37]. In addition, the Ce3d spectrum was recorded. Deconvolution showed that Ce ions were present in a mixed-valence state (~1:2 Ce^{3+}/Ce^{4+}) after sintering under an air atmosphere (Fig. 4D) [38]. Both spectra of Ti 2p species concerning the Ti $2p_{3/2}$ and Ti $2p_{1/2}$ peaks of the LSCNT powders were entirely attributed to the Ti^{4+} valence state.

Ni exsolution at the surface of LSCNT

The crystalline LSCNT powder sintered at 1200 °C for 12 h was placed in an alumina crucible and thermally treated for 10 h under humidified H_2 at 800, 900, 1000, 1100 or 1200 °C. Fig. 5 represents SEM images of the powders after the reduction step. From the SEM images, it is clearly visible that the reduction temperature has a crucial influence on the size, as well as on the amount of the exsolved nanoparticles. For temperatures below 1000 °C, very small nanoparticles (<50 nm) were observed. At higher temperatures, the nickel tended to agglomerate, which resulted in a smaller number of much bigger particles (200–600 nm). The reduction at 800 °C (Fig. 5A) produced the smallest NPs, but also big agglomerates were noticed in the cavities. Based on these observations, to ensure an exsolution of spherical NPs of low dispersity, the reduction temperature was set to 900 °C for all further experiments.

To determine an elementary composition of the fabricated compound, the EDS measurements in the form of point analyses and elemental mapping were performed in an area of uncovered grain (spot P1 marked in Fig. 5C) and exsolved nanoparticles (spot P2 marked in Fig. 5C). The results are presented in Table 2 and Fig. 6, respectively.

As can be seen in Table 2., the area decorated with exsolved nanoparticles was highly enriched with Ni. This proved that the obtained NPs are mostly composed of metallic Ni. The atomic composition of the bare LSCNT obtained from EDS point measurement confirmed the assumed stoichiometry of the compound.

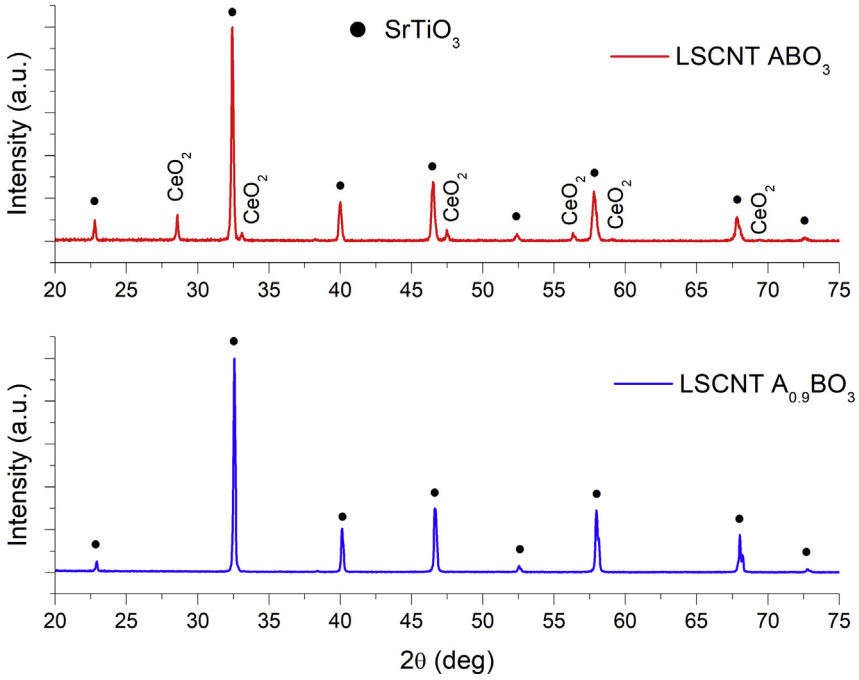

Fig. 3 – XRD patterns of LSCNT with stoichiometry of ABO_3, and $A_{0.9}BO_3$.

Elemental maps taken from the surface of the LSCNT after reduction showed that nickel was highly concentrated in the spots of exsolved NPs. This proved that the obtained segregates were composed of agglomerated metallic nickel. Most interestingly, the Ce ions were also accumulated in the area of the Ni NPs. This could indicate the creation of Ni–Ce or Ni–O–Ce solid solutions. Due to the very low solubility limit of Ce in Ni (<0.1 at.%) [39], and thermodynamics of the creation of Ni–Ce intermetallics [40], the existence of a Ni-doped CeO_2 interlayer between the NPs and the oxide support is more probable [41]. In the case of the SOFC operating under a biogas atmosphere, the observed sockets enriched in cerium are highly desirable. These increase the anti-coking properties, and reduce the agglomeration and sintering of the Ni NPs [42]. This phenomenon occurred most probably thanks to lowering the A-site deficiency after exsolving the nickel from the LSCNT. Cerium ions, which have previously revealed a low tendency towards doping a $SrTiO_3$ lattice, gathered in the nickel-impoverished surface layers just beneath the Ni NPs. Away from the nickel NPs, cerium ions were homogeneously distributed in the surrounding area as well as other elements (O, La, Sr, Ti).

To determine the oxidation states of the elements in the LSCNT after the reduction step, the XPS spectra were collected. The obtained fittings are presented in Fig. 7. They confirm that some nickel was reduced from Ni^{2+} to Ni^0 (Fig. 7A). The observed increase of SrO content was most probably caused due to nickel removal and the reduction of Ti^{4+} to Ti^{3+} (Fig. 7B). Ti^{3+}, as an unstable form of titanium, was hard to identify in the surface layer of the LSCNT powder, but the slight change of peak shape at around 457 eV could be attributed to the formation of the Ti^{3+} state [43]. All of the cerium stayed in an ionic form, and a small increase in the concentration of Ce^{3+} after the reduction step was noticed (see Figs. 4D and 7D).

Table 1 – Lattice parameter of LSCNT unit cell sintered under air at 1200 °C.

Compound	Lattice parameter ($\alpha = \beta = \gamma = 90°$) (Å)	GOF
$SrTiO_3$	3.905 [29]	–
LSCNT	3.898	1.86

Mechanical integration

Dilatometry tests were carried out under an air atmosphere in order to determine the thermal expansion coefficients (TEC) of the LSCNT and the Ni/YSZ anode support applied in the examined fuel cells. The results are presented in Fig. 8A. Both materials were characterised by similar thermal expansion behaviour, which minimises the possibility of cracking and ensures good mechanical integration. A slight deviation from pristine linear expansion for the LSCNT appeared from 600 °C onwards. This phenomena most probably occurred due to the addition of Ce [44]. In fact, the amount of Ce dopant was quite low, and the obtained layer was uniform and without cracks. The SEM image of the LSCNT layer prepared on the SOFC Ni/YSZ anode is presented in Fig. 8B. The adhesion between the Ni/YSZ cermet and the LSCNT was found to be very good, and the catalytic layer was firmly connected to the support. Tests concerning the reaction of the LSCNT with the YSZ electrolyte were performed, and no visible additional phases were observed on the XRD patterns up to 1400 °C.

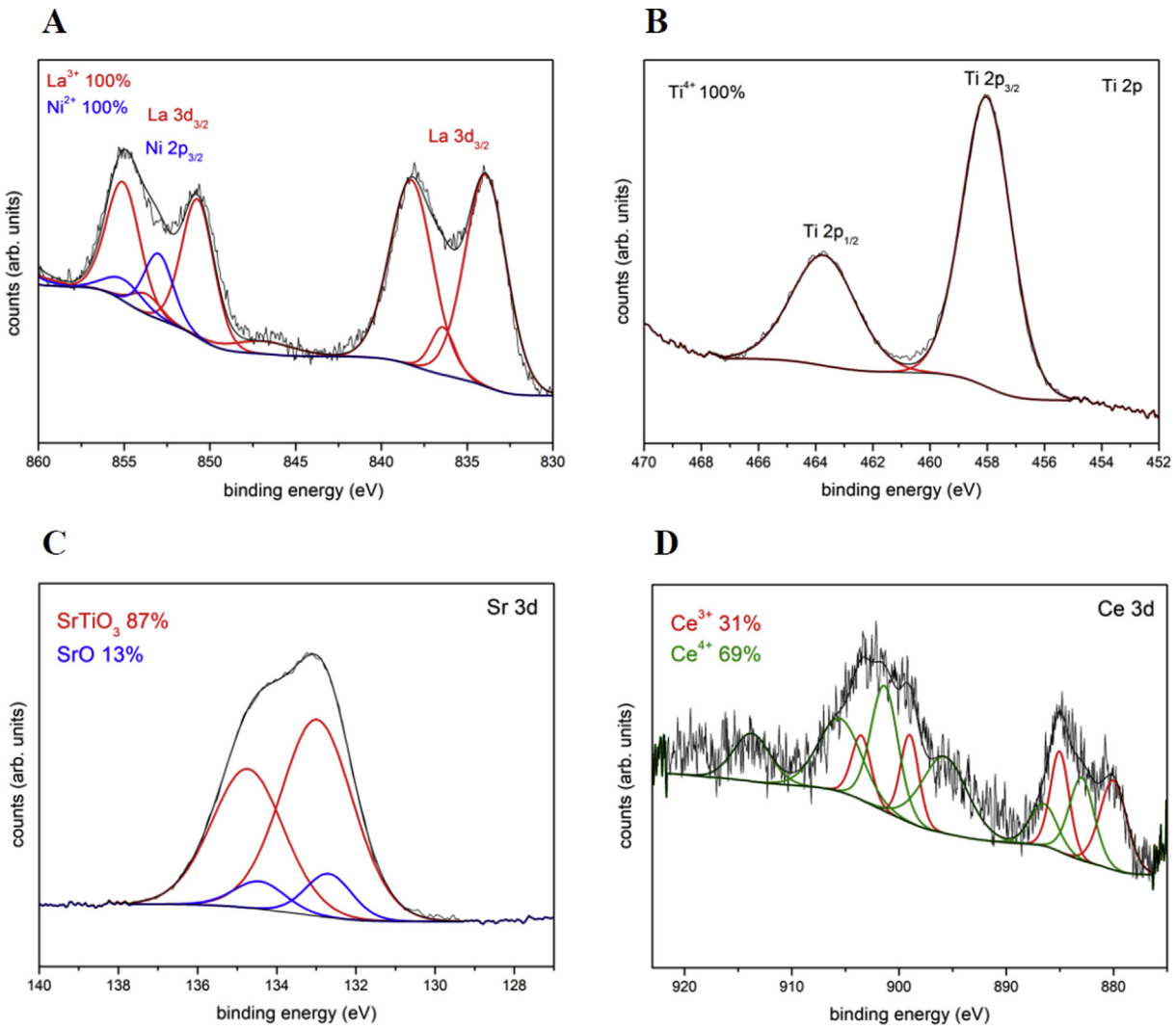

Fig. 4 – XPS spectra of the prepared LSCNT sample: A) La 3d/Ni 2p, B) Ti 2p, C) Sr 3d, and D) Ce 3d.

Electrical tests

In order to perform measurements in SOFC mode, the LSCNT layer was deposited onto the anodic side of a delivered fuel cell. The exsolution process was performed in-situ at 900 °C under humid hydrogen. The results of long-term potentiostatic measurements of the fuel cell fed both with H_2 and synthetic biogas under a static load of 0.65 V are presented in Fig. 9A. For both the reference and the LSCNT-deposited SOFC, a high decrease of current density was observed after switching to biogas stream. This corresponds to a dilution of the fuel stream by side products coming from reforming reactions corresponding to the low fuel utilisation factor, and also to the low quality of the basic SOFC used. During further electrical testing under a biogas atmosphere, a constant increase of current density was observed for both samples within the whole working time. This was most probably caused by momentary slight reoxidation of metallic Ni by water vapour. The low quality of the used SOFC resulted in it taking a long time to reach the current equilibrium point. Relative stability was noticed after around 110 h, and resulted in power densities equal to 327 mA cm^{-2} for the fuel cell with the LSCNT layer and 306 mA cm^{-2} for the reference cell. Fig. 9B and C represent IV plots of the reference and fuel cell with the LSCNT layer after working for 12 h under H_2, and for 130 h under the synthetic biogas mixture.

Both fuel cells had similar performance when operating in pure, humid hydrogen. After feeding them with synthetic biogas for over 130 h, a significantly higher decrease of electrical performance was observed for the reference fuel cell. In the end, the obtained power densities were equal to 199 mW cm^{-2}, and 213 mW cm^{-2} for the reference, and the fuel cell with the LSCNT layer, respectively. Those values corresponded to 15% and 10.5% losses in overall electrical performance compared to the initial power densities under H_2. To sum up, an additional, functional layer of LSCNT

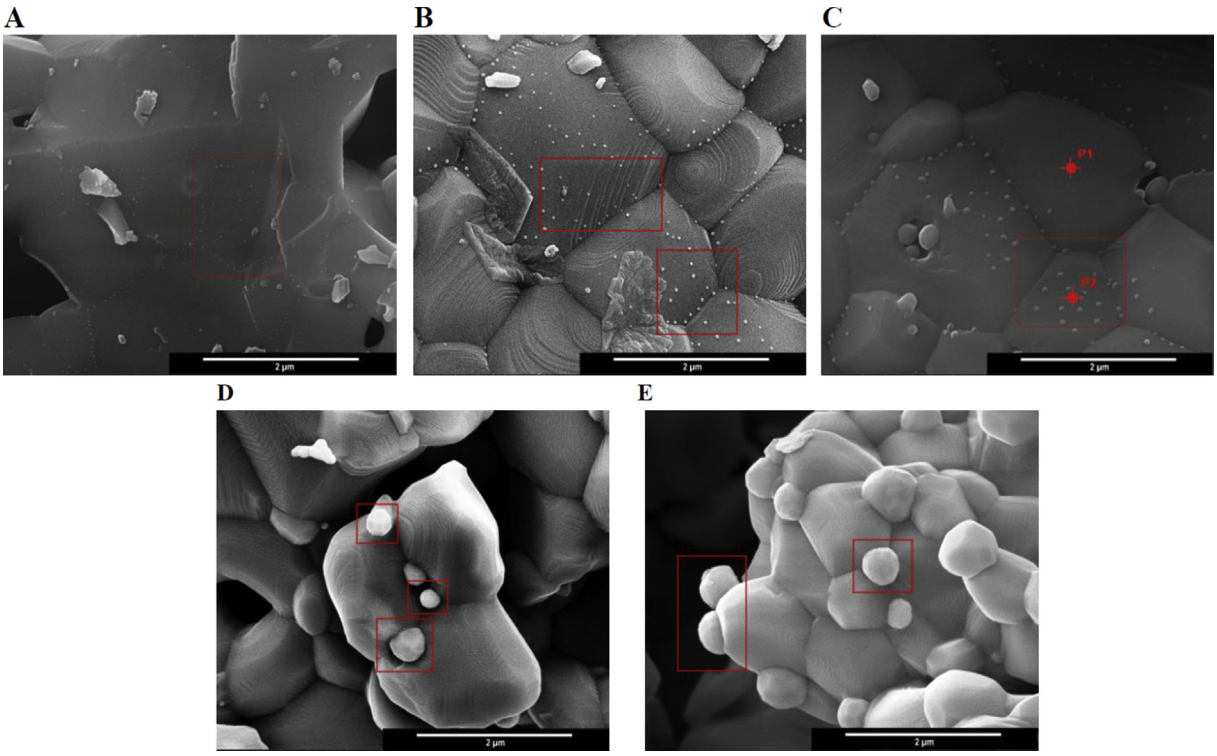

Fig. 5 – SEM images of LSCNT powders reduced at different temperatures. A) 800 °C, B) 900 °C, C) 1000 °C, D) 1100 °C, and E) 1200 °C. Exemplary Ni NPs are marked with red frames. Scale bar is 2 µm. In Fig. 5C, EDS analysis locations are indicated. (For interpretation of the references to color in this figure legend, the reader is referred to the Web version of this article.)

Table 2 – Atomic composition of bare LSCNT grain and exsolved NPs based on EDS results.

Element	at.% bare LSCNT area (spot P1)	at.% NPs area (spot P2)
O	56	41
La	4	2
Sr	8	6
Ce	1	2
Ni	**2**	**19**
Ti	15	13

deposited onto the anodic side of the SOFC provided slightly higher power densities, a higher open-circuit voltage (OCV), and a lower degradation level compared to an unmodified fuel cell. This was most probably caused by reduced carbon accumulation on the surface of the anode, limited nickel sintering, and higher amount of H_2 at the anode coming from biogas reforming reactions. Proving this statement, no carbon deposits were found on the top of the anode of the fuel cell with the LSCNT layer after 130 h of feeding with synthetic biogas (Fig. 11D). This shows that the material exhibited high resistivity against coking.

The results of cyclic tests under 20 ppm of H_2S-contaminated synthetic biogas are presented in Fig. 10.

A very fast deactivation was observed for both tested fuel cells. The current densities decreased quickly after switching to H_2S-contaminated biogas. Slight differences in the deactivation kinetics were noticed between samples only within the first cycle (current density decreased slower for the fuel cell with the LSCNT layer). This effect was most probably caused by the sorption capabilities of the LSCNT layer. It was assumed that the Ni/YSZ cermet composite was extremely unresistant towards sulfur poisoning, and a highly porous layer of LSCNT was not capable of sufficient protection. In contrast to the reference fuel cell, the additional, LSCNT layer ensured much faster recovery and increased current stability after switching back to H_2. When considering the reference fuel cell's degradation level, it went up to 25% of loss in initial current density under H_2, while for the LSCNT-deposited fuel cell, only a 10% loss of performance was observed, even though both fuel cells suffered strongly from deactivation caused by sulfur adsorption and probable formation of Ni_xS_y compounds.

Catalytic activity and kinetics of reforming reactions

To compare the catalytic performance of both tested fuel cells, the parameters such as conversions, yields, and selectivities were calculated, and are depicted in Fig. 11A and B. The *post mortem* SEM images of both anodes are depicted in Fig. 11C and D.

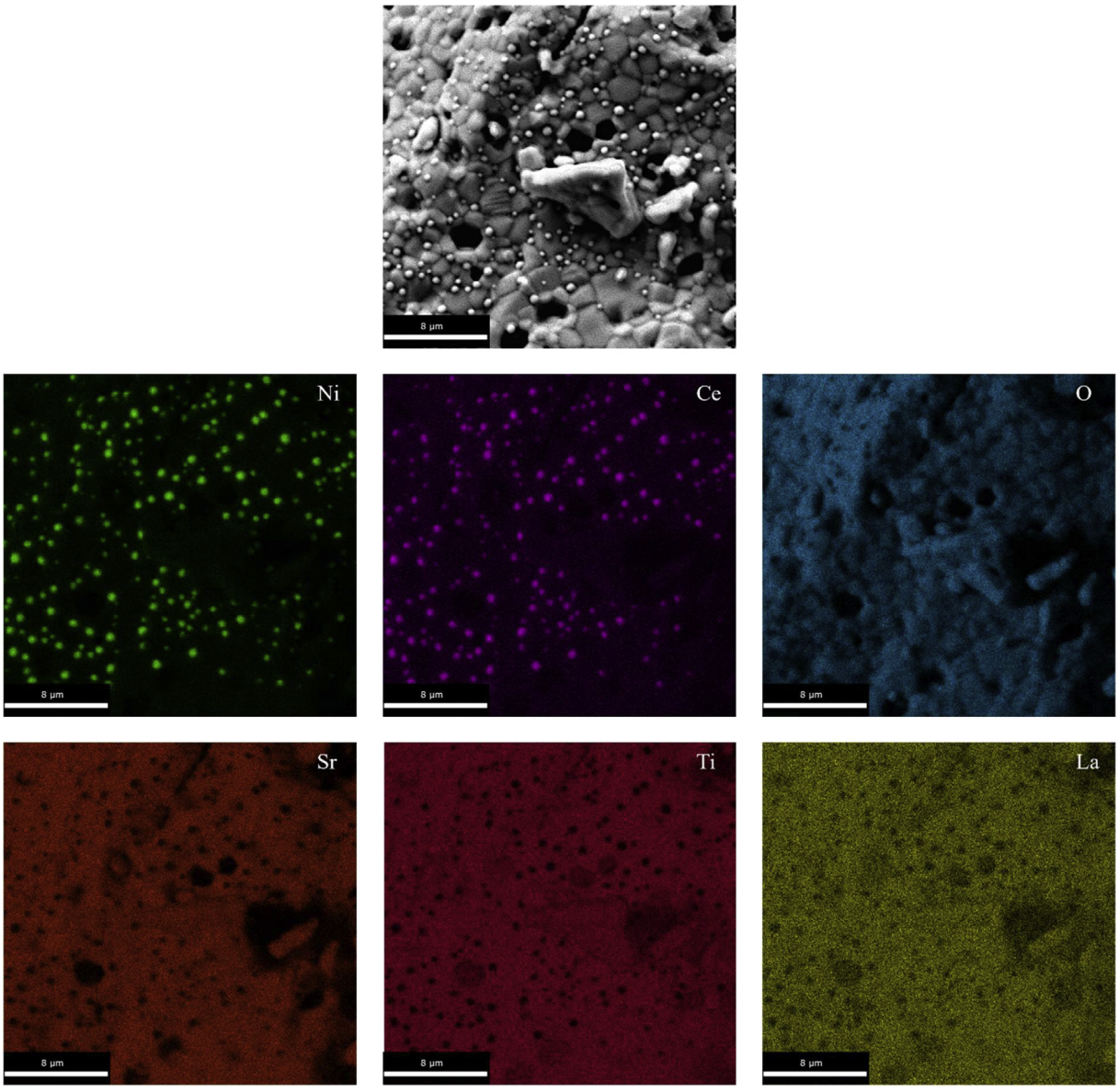

Fig. 6 – EDS elemental map of LSCNT sample reduced at 1200 C under humidified H_2. Magnification 10,000x. Scale bar is 8 μm.

The catalytic parameters obtained for the reference SOFC, which are shown in Fig. 11A, revealed undergoing deactivation and a decrease of catalytic activity of the unprotected anode over the testing period. It was pronounced by a decrease of the CH_4 and CO_2 conversions rates. A lowering of the H_2 yield manifested in a smaller amount of hydrogen in exhaust gases, which was caused by the slowing down of the main reforming processes, and degradation of the anode. The H_2 selectivity of the reference fuel cell decreased during biogas feeding, giving rise to selectivity for CO. In both cases, the selectivity towards CO production was high. This is a normal behaviour observed for Ni-based catalysis of methane reforming [45]. The existence of CO_2 in synthetic biogas feeding mixture even increased the overall CO yield due to parallel undergoing dry reforming (Eq. (1)) and an enhanced RWGS reaction (Eq. (3)). In the case of the fuel cell with the LSCNT layer, the CO selectivity was maintained as stable. At the same time, the results shown in Fig. 11B confirmed the high stability and good catalytic activity towards biogas reforming at the anode with the LSCNT layer. The CH_4 and CO_2 conversion values were much higher than those of the reference fuel cell, and no rapid decrease was observed. All parameters exhibited outstanding stability over the whole SOFC operation under synthetic biogas feeding. Based on the CO selectivity and CO_2 conversion values calculated for the SOFC with the LSCNT layer, it can be assumed that formed CO played a secondary role in the fuel cell electrochemical oxidation, as mentioned before [30]. Lower values of H_2 selectivity for the fuel cell with the LSCNT catalytic layer were a result of a higher level of H_2 electrochemical oxidation

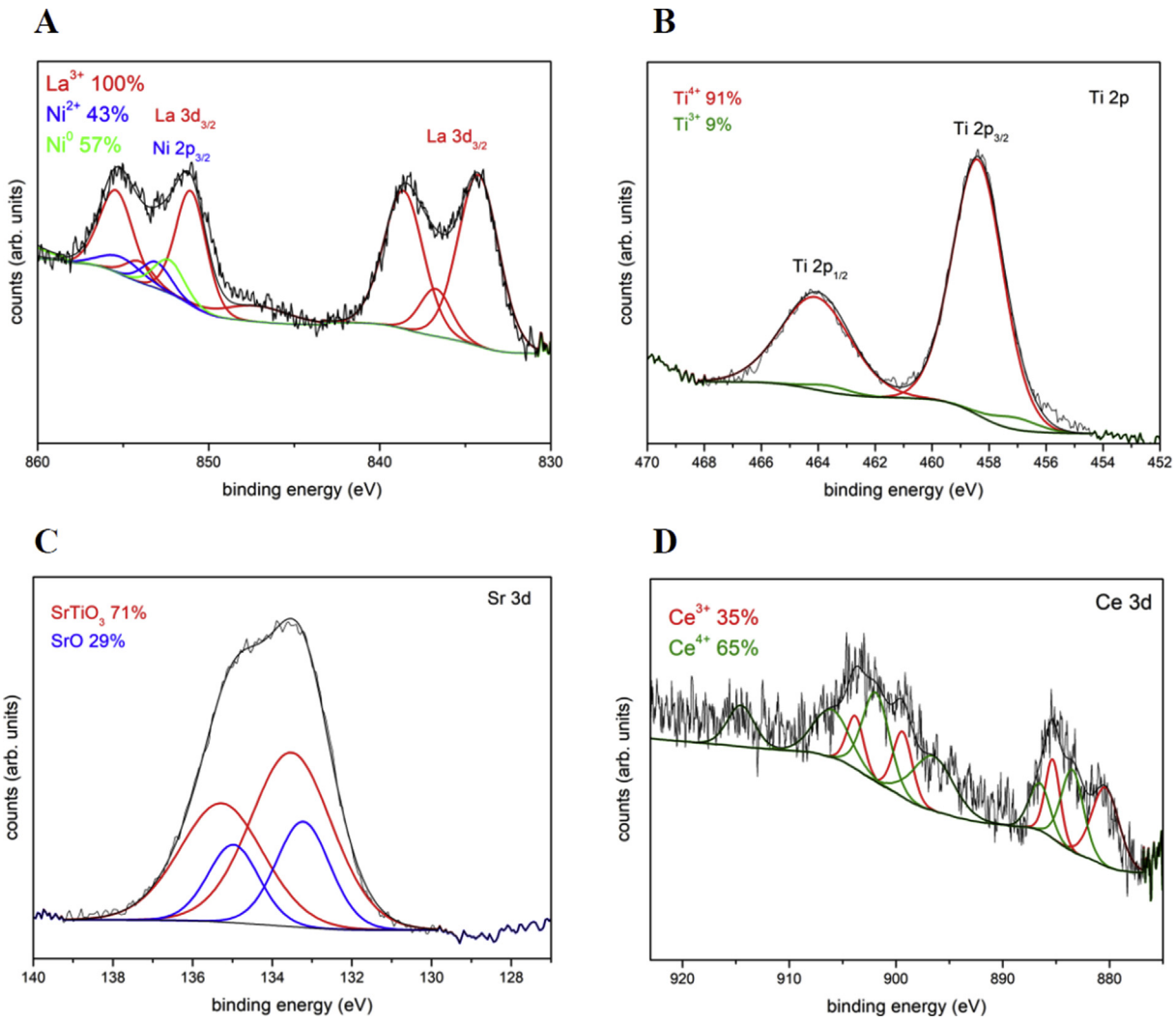

Fig. 7 – XPS spectra of the prepared LSCNT sample after reduction: A) La 3d/Ni 2p, B) Ti 2p, C) Sr 3d, and D) Ce 3d.

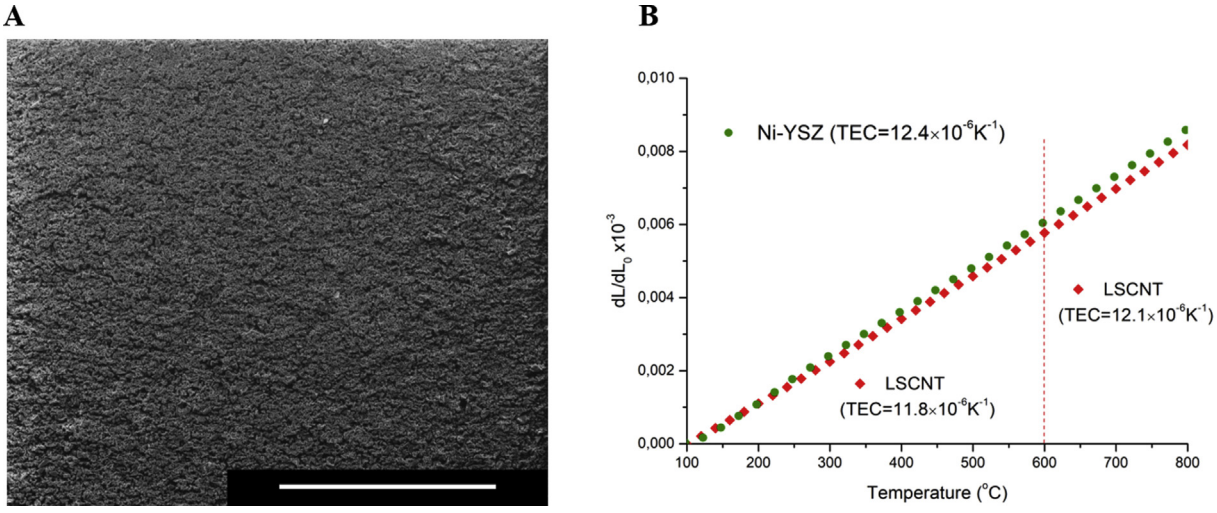

Fig. 8 – A) Sintered layer of LSCNT at Ni/YSZ anode, magnification 100× (scale bar is 500 μm), and B) expansion characteristics of LSCNT and Ni/YSZ anodic material measured under air.

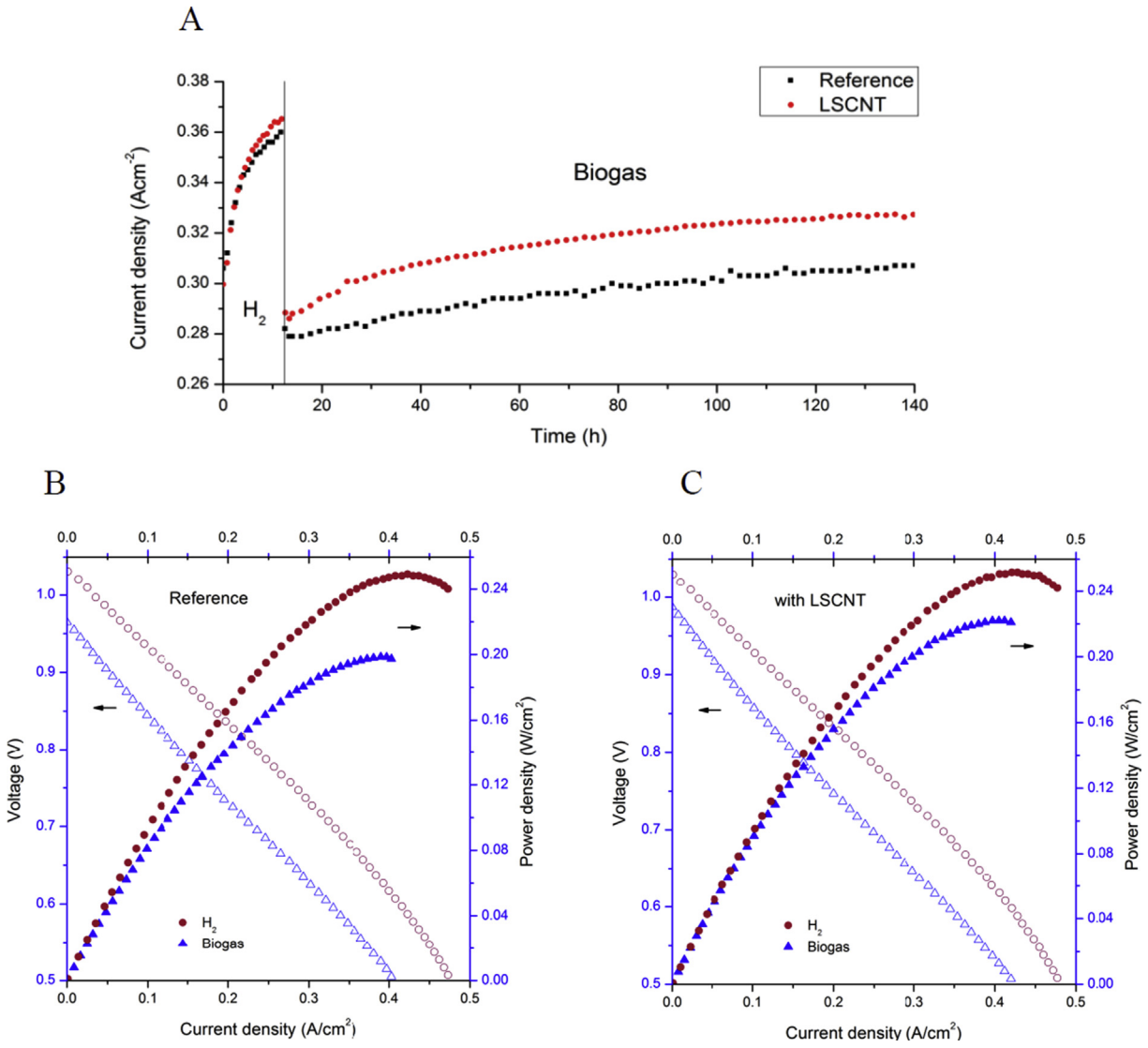

Fig. 9 – Results of electrical measurements for reference and SOFC with LSCNT layer: A) Time-current density, B–C) current density versus voltage (IV) and current density versus power density (IP) curves.

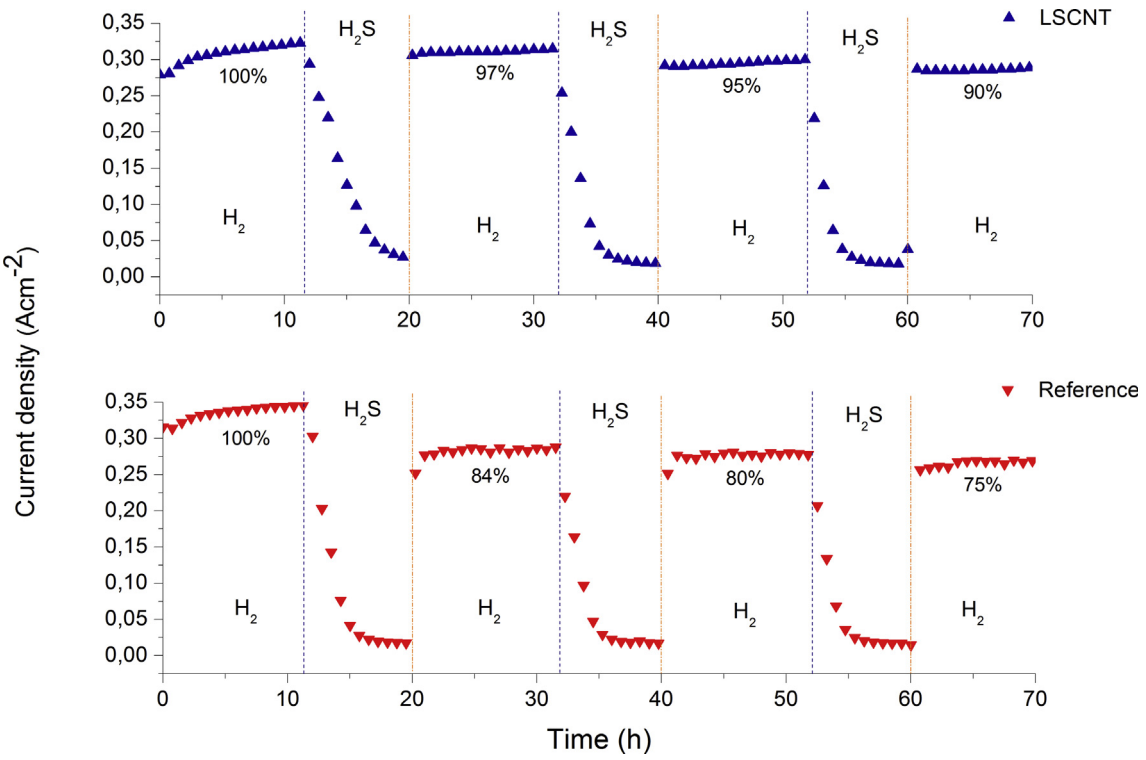

Fig. 10 – Current densities while performing cyclic tests under 20 ppm of H_2S-contaminated biogas and H_2.

compared to the reference sample, and a slightly lower amount of metallic nickel available for reaction. Carbon accumulates were found after 130 h of biogas feeding only at the anode of the reference fuel cell (Fig. 11C). The LSCNT layer was fully free of coke deposits (Fig. 11D), but at the same time, a slight increase in the nickel NP size was observed. This was most probably caused by nickel diffusion through the surface, and via the creation of nickel carbonyl compounds. Additionally, due to the low utilisation factor, the anode was constantly facing the reductive atmosphere, so the exsolution process could still continue, resulting in an increase in the size of the segregated nanoparticles.

Even though, there are many other catalysts for methane reforming exhibiting higher selectivities and conversions [46,47], the main driving force for further development of the proposed compound is its great mechanical integrity with other components of SOFCs, and its outstanding long-term catalytic stability.

Time-dependent values of Q_r and $\alpha_{C,r}$ obtained for the reference SOFC, and the fuel cell with the LSCNT layer are presented in Fig. 12. Based on the obtained results, it was confirmed that steam reforming (Eq. (2)) was a dominating reaction. That was due to the existence of a high amount of water vapour in the reaction chamber. For both tested SOFCs, steam and dry reforming reactions were fully directed towards products thanks to the high temperature and presence of nickel.

When considering the reference fuel cell, it was clearly visible that the Q_r values for dry as well as steam reforming were decreasing during the testing time, which clearly showed a loss of overall catalytic efficiency. The better performance of the fuel cell with the layer LSCNT was pronounced by a stable increase in values of Q_r with a low slope during the work under the biogas stream. A higher slope of steam reforming Q_r change revealed that this reaction certainly dominated the dry reforming. The RWGS reaction in both cases was located somewhere nearby equilibrium point ($Q_r = 1$) as this process is extremely fast and cannot be avoided.

For the reference SOFC, the Q_r parameter of RWGS oscillated around lower values than for the LSCNT-deposited fuel cell. This introduced a slightly negative, parasitic character of RWGS reaction resulting in CO_2 to CO conversion with parallel consumption of H_2. A methanation reaction for both fuel cells was shifted to the site of the substrates. This means that the methanation reaction was with high probability encouraged into water-assisted H_2 production.

When considering the reactions that could cause anode coking (Eq (5)–(7)), the carbon accumulation was most probably promoted by methane pyrolysis ($\alpha_{C,r} > 1$). A non-equilibrium analysis also revealed that the SOFC with the deposited LSCNT layer had higher activity toward carbon gasification, and higher reaction stability compared to the unmodified SOFC. This was assumed by a much lower change of the Q_r values for both the Boudouard reaction, and the CO reduction so the dynamics of equilibrium shifting was less pronounced than for the reference SOFC.

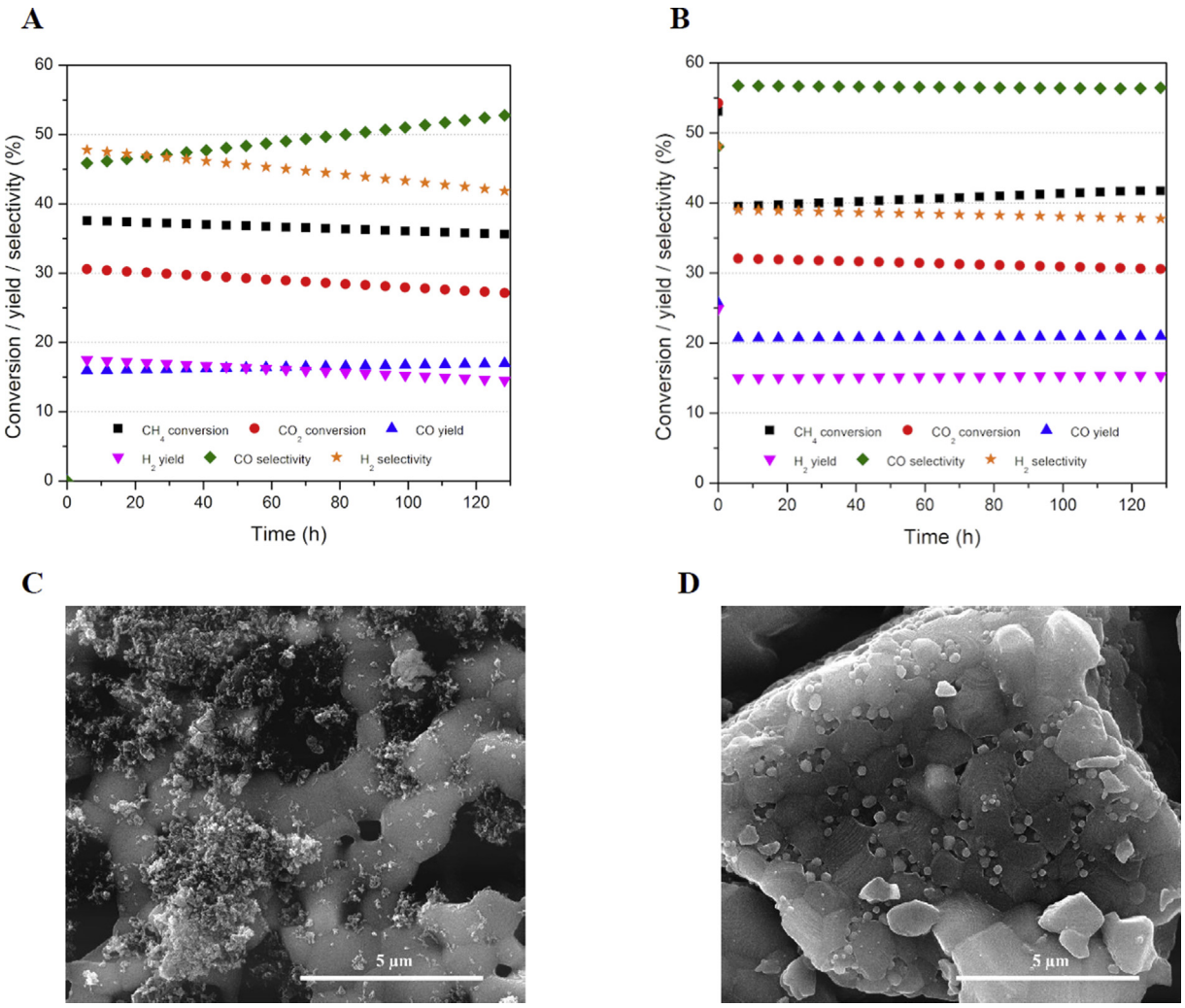

Fig. 11 – Catalytic parameters of reforming reactions and *post mortem* SEM image of anode: A, C) reference, and B, D) fuel cell with LSCNT layer.

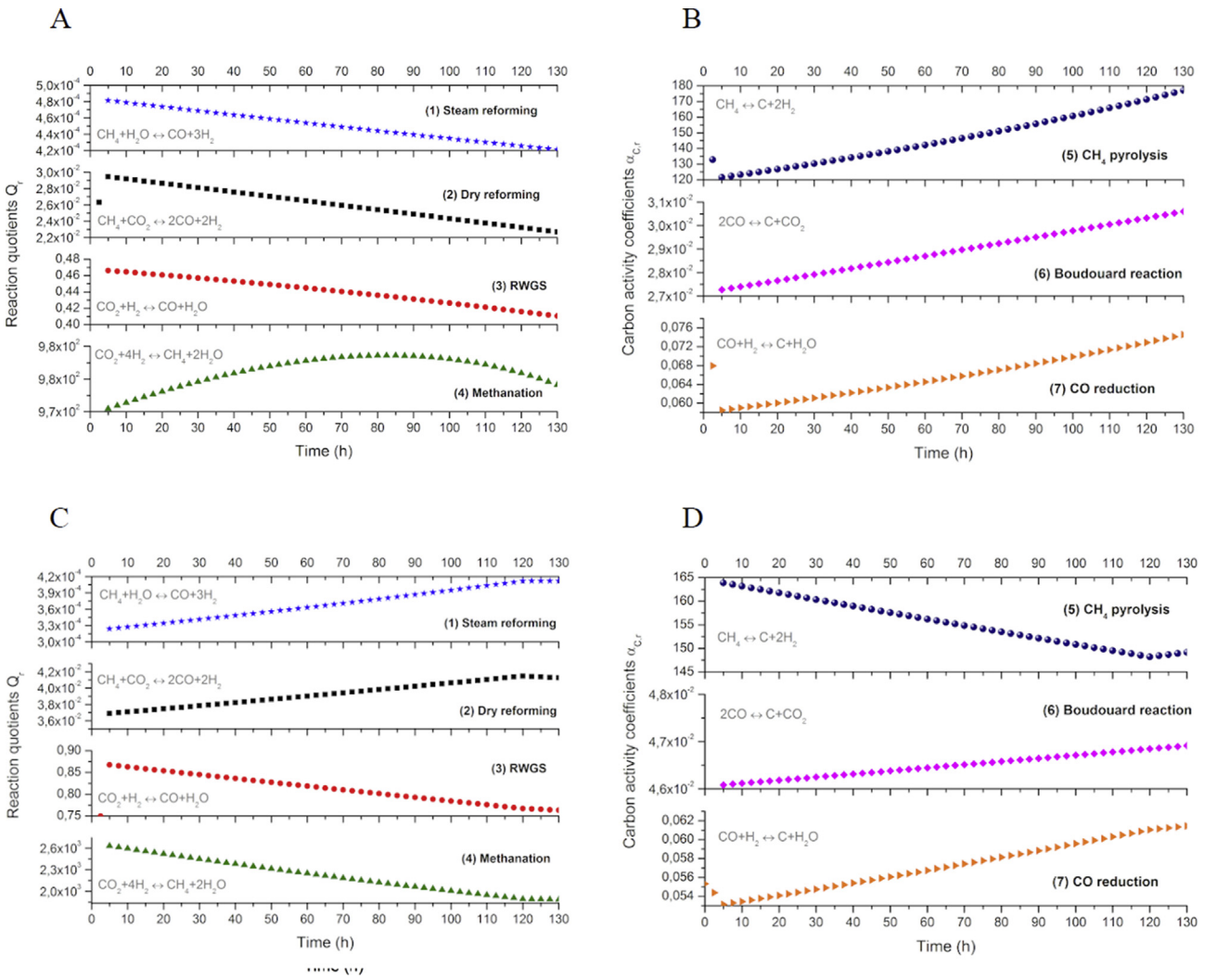

Fig. 12 – Reaction quotients Q_r (left), and $\alpha_{C,r}$ (right) calculated for: A–B) reference fuel cell, and C–D) SOFC with LSCNT layer.

Conclusions

The purpose of this work was to synthesise a new catalytic material based on $SrTiO_3$ perovskite by co-doping with La, Ce, and Ni. A compound of general formula $La_{0.27}Sr_{0.54}Ce_{0.09}Ni_{0.1}Ti_{0.9}O_{3-\sigma}$ (LSCNT) was obtained using the Pechini method. The XRD and SEM/EDS measurements proved that after sintering at 1200 °C, it was possible to fabricate a single-phase material with the desired stoichiometry. After the reduction step at 900 °C, Ni ions exsolved at the surface of the LSCNT in the form of spherical nanoparticles with an average size of around 22 nm.

Long-term stability tests of a single-cell unit in synthetic and H_2S-contaminated biogas were performed. The fuel cell with a layer of LSCNT deposited onto the anodic side resulted in much better stability, and produced higher current densities over the whole testing time while working under pure, synthetic biogas. A cyclic test of the SOFC in biogas containing 20 ppm of H_2S revealed that both samples underwent full deactivation. Even though, anode with the LSCNT ensured higher performance recovery.

A non-equilibrium analysis of the reforming reactions provided information about the direction of each from parallel processes. It was assumed that steam reforming plays a major role in H_2 generation in both the reference, and the fuel cell with the LSCNT layer. Applying LSCNT on the anodic side of the SOFC increased the stability and catalytic activity of the fuel cell while working under synthetic biogas stream. The presented material is a promising candidate for further research into LSCNT-supported DIR-SOFCs.

Declaration of competing interest

The authors declare that they have no known competing financial interests or personal relationships that could have appeared to influence the work reported in this paper.

Acknowledgement

This work was supported by the National Science Centre, Poland under grant No. NCN 2017/26/D/ST8/00822.

REFERENCES

[1] Milani D. Renewable energy integration in combined cooling, heating, and power (CCHP) processes, polygeneration with polystorage energy and chemical hubs, Chapter: 14. Elsevier; 2018. p. 459–91.
[2] Stambouli AB, Traversa E. Solid oxide fuel cells (SOFCs): a review of an environmentally clean and efficient source of energy, Renewable and Sustainable Energy Reviews, Chapter: 6. Elsevier; 2002. p. 433–55.
[3] Hagen A, Winiwarter A, Langnickel H, Johnson G. SOFC operatiomln with real biogas, fuel cells, Chapter: 17. John Wiley & Sons; 2017. p. 854–61.
[4] Huang K, Goodenough JB. Solid Oxide Fuel Cell Technology: Principles, Performance and Operations. Woodhead Publishing; 2009. Series in Energy, Solid Oxide Fuel Cell Technology, Woodhead Publishing.
[5] Gupta N, Yadav GD. Solid Oxide Fuel Cell: A Review. IRJET; 2016. p. 1006–11.
[6] Wang K, Hissel D, Péra MC, Steiner N, Marra D, Sorrentino M, Pianese C, Monteverde M, Cardone P, Saarinen J. A Review on solid oxide fuel cell models. Int J Hydrogen Energy 2011;36:7212–28. https://doi.org/10.1016/j.ijhydene.2011.03.051.
[7] Mahato N, Banerjee A, Gupta A, Omar S, Balani K. Progress in material selection for solid oxide fuel cell technology: a review. Prog Mater Sci 2015;72:141–337. https://doi.org/10.1016/j.pmatsci.2015.01.001.
[8] Xianhui Z, Babu J, John K, Soydan O. Biogas reforming to syngas: a review. iScience 2020;23. https://doi.org/10.1016/j.isci.2020.101082.
[9] Shiratori Y, Oshima T, Sasaki K. Feasibility of direct-biogas SOFC. Int J Hydrogen Energy 2008;33:6316–21. https://doi.org/10.1016/j.ijhydene.2008.07.101.
[10] Papurello D, Lanzini A. SOFC single cells fed by biogas: experimental tests with trace contaminants. Waste Manag 2018;72:306–12. https://doi.org/10.1016/j.wasman.2017.11.030.
[11] Chlipała M, Błaszczak P, Wang S-F, Jasiński P, Bochentyn B. In situ study of a composition of outlet gases from biogas fuelled Solid Oxide Fuel Cell performed by the Fourier Transform Infrared Spectroscopy. Int J Hydrogen Energy 2019;44:13864–74. https://doi.org/10.1016/j.ijhydene.2019.03.243.
[12] Boldrin P, Ruiz-Trejo E, Mermelstein J, Bermúdez JM, Reina TR, Brandon NP. Strategies for carbon and sulfur tolerant solid oxide fuel cell materials, incorporating lessons from heterogeneous catalysis. Chem Rev 2016;116:13633–84. https://doi.org/1021/acs.chemrev.6b00284.
[13] Hansen JB. Chapter 13 - Direct Reforming Fuel Cells, Fuel Cells: Technologies for Fuel Processing. Elsevier; 2011. p. 409–50. https://doi.org/10.1016/B978-0-444-53563-4.10013-6.
[14] Mehran MT. Improving sulfur tolerance of Ni-YSZ anodes of solid oxide fuel cells by optimization of microstructure and operating conditions. Int J Hydrogen Energy 2018;43:11202–13. https://doi.org/10.1016/j.ijhydene.2018.04.200.
[15] Zhu T, Troiani H, Mogni LV, Santaya M, Han M, Barnett SA. Exsolution and electrochemistry in perovskite solid oxide fuel cell anodes: role of stoichiometry in Sr(Ti,Fe,Ni)O_3. J Power Sources 2019;439. https://doi.org/10.1016/j.jpowsour.2019.227077.
[16] Kobsiriphat W, Madsen BD, Wang Y, Shah M, Marks LD, Barnett SA. Nickel- and ruthenium-doped lanthanum chromite anodes: effects of nanoscale metal precipitation on solid oxide fuel cell performance. J Electrochem Soc 2010;157. https://doi.org/10.1149/1.3269993.
[17] Kamecki B, Miruszewski T, Górnicka K. Characterization methods of nickel nano-particles obtained by the ex-solution process on the surface of Pr, Ni-doped $SrTiO_3$ perovskite ceramics. SN Applied Sciences 2019;1:322. https://doi.org/10.1007/s42452-019-0317-7.
[18] Madsen BD, Kobsiriphat W, Wang Y, Marks LD, Barnett SA. Nucleation of nanometer-scale electrocatalyst particles in solid oxide fuel cell anodes. J Power Sources 2007;166:64–7. https://doi.org/10.1016/j.jpowsour.2006.12.080.
[19] Neagu D, Irvine JTS. Structure and properties of $La_{0.4}Sr_{0.4}TiO_3$ ceramics for use as anode materials in solid oxide fuel cells. Chem Mater 2010;22:5042–53. https://doi.org/10.1021/cm101508w.
[20] Neagu D, Irvine JTS, Irvine. Enhancing electronic conductivity in strontium titanates through correlated A and B-site doping. Chem Mater 2011;23:1607–17. https://doi.org/10.1021/cm103489r.
[21] Kolodiazhnyi T, Petric A. The applicability of Sr-deficient n-type $SrTiO_3$ for SOFC anodes. J Electroceram 2005;15:5–11. https://doi.org/10.1007/s10832-005-0375-7.
[22] Atkinson A, Barnett SA, Gorte R, Irvine J, Mcevoy A, Mogensen M, Singhal CA Sourabh, Vohs J. Advanced anodes for high-temperature fuel cells. Nat Mater 2004;3:17–27. https://doi.org/10.1038/nmat1040.
[23] Neagu D, Oh TS, Miller DN, Ménard H, Bukhari SM, Gamble SR, Gorte RJ, Vohs JM, Irvine JTS. Nano-socketed nickel particles with enhanced coking resistance grown in situ by redox exsolution. Nat Commun 2015;6:8120. https://doi.org/10.1038/ncomms9120.
[24] Périllat-Merceroz C, Gauthier G, Roussel P, Huvé M, Gélin P, Vannier R-N. Synthesis and study of a Ce-doped La/Sr titanate for solid oxide fuel cell anode operating directly on methane. Chem Mater 2011;23:1539–50. https://doi.org/10.1021/cm103316b.
[25] Sun Y, Zhou X, Zeng Y, Amirkhiz BS, Wang M, Zhang L, Hua B, Li J, Li J, Luo J. An ingenious Ni/Ce co-doped titanate based perovskite as a coking-tolerant anode material for direct hydrocarbon solid oxide fuel cells. J Mater Chem A 2015;3:22830–8. https://doi.org/10.1039/C5TA06200D.
[26] Georges S, Bailly N, Steil C, Bultel Y, Hadjar A. SOFC long term operation in pure methane by gradual internal reforming. Electrochemical Society 2013;57(1):3023–30. https://doi.org/10.1149/05701.3023ecst.
[27] van Biert L, Godjevac M, Visser K, Aravind PV. Dynamic modelling of a direct internal reforming solid oxide fuel cell stack based on single cell experiments. Appl Energy 2019;250:976–90. https://doi.org/10.1016/j.apenergy.2019.05.053.
[28] Granada E, Eguıa P, Vilan JA, Comesana JA, Comesana R. FTIR quantitative analysis technique for gases, Application in a biomass thermochemical process. Renew Energy 2012;41:416–21. https://doi.org/10.1016/j. renene.2011.11.020.
[29] Speitel LC. Fourier transform infrared analysis of combustion gases. J Fire Sci 2002. https://doi.org/10.1177/073490410202005484.
[30] Klein JM, Hénault M, Roux C, Bultel Y, Georges S. Direct methane solid oxide fuel cell working by gradual internal steam reforming: analysis of operation. J Power Sources 2009;193:331–7.
[31] Presto S, Barbucci A, Carpanese MP, Han F, Costa R, Viviani M. Application of La-doped SrTiO3 in advanced

metal-supported solid oxide fuel cells. Crystals 2018;8:134. https://doi.org/10.3390/cryst8030134.
[32] Shannon RD. Revised Effective Ionic Radii and Systematic Studies of Interatomic Distances in Halides and Chalcogenides, Central Research and Development Department, Experimental Station, E. I. Du Pont de Nemours and Company, Wilmington, Delaware 19898, U.S.A. Acta Crystallogr 1976.
[33] Anderson J, Bharat J, Stemmer S, Van de Walle C. Effects of doping on the lattice parameter of SrTiO3. Appl Phys Lett 2012;100:262104. https://doi.org/10.1063/1.4730998.
[34] Vasquez RP. SrTiO3 by XPS, Surface Science Spectra. 1992. p. 129–35. https://doi.org/10.1116/1.1247683.
[35] Rodenbücher C. Resistive Switching Phenomena of Extended Defects in Nb-doped SrTiO3 under Influence of External Gradients. In: Forschungszentrum Jülich GmbH Zentralbibliothek, Verlag, Reihe Information. 38; 2014, ISBN 978-3-89336-980-5.
[36] Bachelet R, Sanchez F, Palomares F, Ocal C. Atomically flat SrO-terminated $SrTiO_3$(001) substrate. Appl Phys Lett 2009;95:141915. https://doi.org/10.1063/1.3240869. 141915.
[37] Hensling F, Baeumer C, Rose MA, Gunkel F, Dittmann R. $SrTiO_3$ termination control: a method to tailor the oxygen exchange kinetics. Materials Research Letters 2020;8:31–40. https://doi.org/10.1080/21663831.2019.1682705.
[38] Górnicka K, Carnicom EM, Gołąb S, Łapiński M, Wiendlocha B, Xie W, Kaczorowski D, Cava RJ, Klimczuk T. $CeIr_3$: superconductivity in a phase based on tetragonally close packed clusters. Supercond Sci Technol 2019;32. https://doi.org/10.1088/1361-6668/aaf48f.
[39] Goodall R. Data of the maximum solid solubility limits of binary systems of elements. Data in Brief 2019;26. https://doi.org/10.1016/j.dib.2019.104515.
[40] Ivanov MI, Berezutskii VV, Shevchenko MO, Subotenko PM, Kudin VG, Sudavtsova VS. Thermodynamic Properties of Ce–Ni Binary Alloys. Powder Metall Met Ceram 2016;54(9–10):590–8. https://doi.org/10.1007/s11106-016-9752-9.
[41] Ay H, Uner D. Dry reforming of methane over CeO_2 supported Ni, Co and Ni–Co catalysts. Appl Catal B Environ 2015;179. https://doi.org/10.1016/j.apcatb.2015.05.013.
[42] Huaiyu Z, Wei W, Ran R, Zongping S. A new nickel–ceria composite for direct-methane solid oxide fuel cells. Int J Hydrogen Energy 2013;38:3741–9. https://doi.org/10.1016/j.ijhydene.2013.01.032.
[43] Atuchin VV, Kesler VG, Pervukhina NV, Zhang Z. Ti 2p and O 1s core levels and chemical bonding in titanium-bearing oxides. J Electron Spectrosc Relat Phenom 2006;152(1–2):18–24. https://doi.org/10.1016/j.elspec.2006.02.004.
[44] Iqbal RM, Nurherdiana SD, Sahasrikirana MS, Harmelia L, Utomo WP, Setyaningsih EP, Fansuri H. The Compatibility of NiO, CeO_2 and NiO-CeO_2 as a Coating on $La_{0.6}Sr_{0.4}Co_{0.2}Fe_{0.8}O_{3-\delta}$, $La_{0.7}Sr_{0.3}Co_{0.}Fe_{0.8}$ $O_{3-\delta}$ and $La_{0.7}Sr_{0.3}Mn_{0.3}O_{3-\delta}$ Ceramic Membranes and Their Mechanical Properties. IOP Conf Ser Mater Sci Eng 2018;367. https://doi.org/10.1088/1757-899X/367/1/012032.
[45] Meloni E, Martino M, Palma V. A Short Review on Ni Based Catalysts and Related Engineering Issues for Methane Steam Reforming. Catalysts 2020;10:352. https://doi.org/10.3390/catal10030352.
[46] Angeli S, Turchetti L, Monteleone G, Lemonidou A. Catalyst development for steam reforming of methane and model biogas at low temperature. Appl Catal B Environ 2015;181. https://doi.org/10.1016/j.apcatb.2015.07.039.
[47] Shi N, Xie Y, Yang Y. Review of anodic reactions in hydrocarbon fueled solid oxide fuel cells and strategies to improve anode performance and stability. Mater Renew Sustain Energy 2020;9. https://doi.org/10.1007/s40243-020-0166-8.